Construction and Building Materials 311 (2021) 125338

Contents lists available at ScienceDirect

Construction and Building Materials

journal homepage: www.elsevier.com/locate/conbuildmat

Characterizing damage modes and size effects in high-strength concrete under hydrostatic and triaxial stress states using X-ray microtomography

Brett Williams [a,b,*], Anna Madra [c], William Heard [a], Steven Graham [a], Michael Grotke [a], Michael Hillman [c], Xu Nie [b]

[a] Engineer Research and Development Center, 3909 Halls Ferry Rd., Vicksburg, MS 39180, USA
[b] Southern Methodist University, Mechanical Engineering, 3101 Dyer Street, Dallas, TX 75205, USA
[c] Pennsylvania State University, Civil and Environmental Engineering, 212 Sackett Building, University Park, PA 16802, USA

ARTICLE INFO

Keywords:
High-strength concrete
Triaxial loading
X-ray microtomography
Damage segmentation
Size effects

ABSTRACT

Damage modes are drastically different for concrete under complex stress states. This study investigates damage in high-strength concrete under triaxial loading with confinement pressures up to 200 MPa, while also considering effects from changes in specimen length-to-diameter ratio. Damage was observed and segmented using X-ray microtomography. Hydrostatic pressures up to 200 MPa were fully reversible and caused no detectable damage, thus triaxial deviator stresses dictated damage extent. Brittle failure modes produced shear cracks at angles of 25-30° that became more distributed with increased confinement. Ductile failure modes observed pore collapse with residual strengths being ~30–50% of pristine strengths.

1. Introduction

Under a penetration event with multiple impacts, it is critical to know the state of damaged material in order to have predictive capabilities for subsequent impacts. This problem has proven to be very challenging for Department of Defense (DoD) researchers due to the very limited knowledge on pressure-dependent damage evolution for high-strength concrete. In order to improve modeling capabilities, researchers have extensively investigated damage and fracture processes of brittle materials [1–6]. Through the use of nondestructive X-ray microtomography (micro-CT), internal damage can be documented in three dimensions to better understand complex cracking and fracture patterns [7]. Rather than solely using a statistical distribution to describe flaws and damage, micro-CT provides a method to precisely characterize physical damage to better understand crack nucleation and propagation within the various phases of brittle geomaterials [8].

Through the development of high-resolution micro-CT, heterogeneities at small length scales can be precisely visualized and characterized allowing for better understanding of crack nucleation and propagation within complex geomaterials [8]. Cnudde and Boone provide a thorough review of the history of micro-CT as it relates to geosciences to include advantages, limitations, artifacts, and operator dependencies [9]. Although large CT systems had previously been used for concrete [10], Landis et al. were some of the pioneers for utilizing micro-CT to investigate cementitious materials as he worked toward providing a physical basis for a scalar damage variable [11]. Many models incorporate a scalar damage variable that describes damage simply from zero (pristine) to one (fully damaged). However, the implementation of damage parameters is more effective if related to physical observations and measurements. Landis et al. used synchrotron radiation to map 3D crack morphology of loaded concrete cylinders (4 mm ×4 mm) with an initial voxel resolution of 6 μm [12–13] that later improved to 1.2 μm [14]. Researchers have also been pairing micro-CT studies with digital image correlation (DIC) [15] and eventually digital volume correlation (DVC) to measure displacements within heterogeneous materials to evaluate strain fields [16]. Micro-CT has provided valuable insight to concrete researchers in terms of damage progression under compression [3,17–18] and splitting tension [4,19], porosity measurements [20], damage morphology from thermal effects [21], and self-healing [22]. A thorough review of micro-CT research as it relates specifically to cementitious materials has been documented by Brisard et al. [23].

Although pressure-dependent material properties of high-strength concretes have been thoroughly documented [24–27], micro-CT has been used infrequently for investigating specimens undergoing high-pressure triaxial loadings. Unfortunately, in situ micro-CT scans of specimens under high confining pressure (200 MPa) is not feasible, since

* Corresponding author at: Engineer Research and Development Center, 3909 Halls Ferry Rd., Vicksburg, MS 39180, USA.
E-mail address: Brett.A.Williams@erdc.dren.mil (B. Williams).

https://doi.org/10.1016/j.conbuildmat.2021.125338
Received 27 August 2021; Received in revised form 18 October 2021; Accepted 20 October 2021
Available online 28 October 2021
0950-0618/Published by Elsevier Ltd.

pressure vessels are not X-ray transparent. Some studies have used ex situ scans to characterize triaxial damage modes for unloaded specimens made from conventional-strength concrete containing coarse aggregates [28]. However, to the best of the authors' knowledge, triaxial damage states have not been investigated for high-strength concretes that do not contain coarse aggregates. Furthermore, prior investigations using micro-CT for triaxial damage studies have not included volumetric strain measurements.

This study aims to assess the damage evolution of high-strength concrete under hydrostatic and triaxial stress states with confining pressures up to 200 MPa to capture brittle, quasi-brittle, and ductile failure modes. Furthermore, this study investigates specimens with a reduced length-to-diameter ratio (L/D), since these specimen geometries are required for dynamic triaxial experiments [29]. Triaxial experiments were performed using a sealed specimen with hydrostatic fluid pressure maintained in the radial direction while an additional axial load is applied by a hydraulic actuator. In-situ volumetric strains were calculated using vertical linear variable differential transformers (LVDTs) and a radial strain sensor with removable mounts. A high-resolution laboratory micro-CT scanner was implemented to non-destructively view and analyze pristine and damaged concrete specimens. The resulting micro-CT scans allow for damage visualization and measurements in terms of bulk volumetric strains, shear planes, crack saturation, and the evolution of pore size distributions. Additionally, residual strength measurements provide a method to connect damage morphologies to quantifiable material properties.

2. Material and methods

2.1. Material and specimen preparation

A high-strength self-consolidating concrete referred to as BBR9 was selected for all of the testing and characterization presented in this study. BBR9 has been previously documented in the literature to include design philosophy [30] and mechanical performance [31–34]. Damage modes have also been investigated for unconfined compression experiments at high strain rates [17]. The mixture proportion for BBR9 is presented in Table 1 consisting of the following constituent materials, i.e., manufactured limestone sand, type I/II portland cement, grade-100 ground granulated blast-furnace slag (GGBFS), undensified microsilica (silica fume), polycarboxylate-ether-based high-range water-reducing admixture (HRWRA), and tap water. The concrete contains no coarse aggregate, and the fine aggregate (sand) has a maximum particle size of 4.75 mm.

Cylindrical specimens with a diameter of 25.4 mm were cored from bulk samples in accordance with ASTM C 42 [35]. A precision saw was used to cut the specimens slightly longer than the desired length. The final specimen lengths of 25 mm and 50 mm were achieved using a PR Hoffman PR-1 85 T double-sided planetary lapping machine resulting in parallelism and flatness within 25 μm. Pristine BBR9 specimens are shown in Fig. 1.

Table 1
Mixture proportions for BBR9 high-strength concrete.

Constituent	Mixture Proportions, by Weight	Specific Gravity
Cement (Type I-II)	1.00	3.15
Manufactured limestone sand	2.25	2.57
Slag	0.60	2.95
Microsilica (silica fume)	0.26	2.20
Tap water	0.37	1.00
High-range water-reducing admixture	0.03	1.20

Fig. 1. Pristine cylindrical BBR9 high-strength concrete specimens with L/D = 2.0 (left) and L/D = 1.0 (right).

2.2. Quasi-static hydrostatic and triaxial compression

The quasi-static hydrostatic and triaxial test equipment is detailed in the literature [25,36–37]. An in-depth review of the quasi-static triaxial testing on 25-mm-diameter BBR9 concrete specimens is presented in previously published work [38]. As a brief overview, the cylindrical concrete specimen is sealed with fluid pressure being applied to the entire specimen to achieve a hydrostatic stress state. For the triaxial loading, the desired level of fluid confinement pressure is held constant in the radial direction while an actuator loads the specimen in the axial direction. Furthermore, a MoS_2-based lubricant is applied at the specimen/platen interface to reduce frictional end effects.

All results in this study are presented in terms of true (Cauchy) stress through active monitoring of the specimen's cross-sectional area using a centrally located LVDT-based lateral deformeter with removable gauge mounts. The principal true stress difference (q) is defined by the difference between axial stress (σ_a, or σ_3) and radial stress (σ_r, or σ_1 and σ_2), as shown in Eq. (1), and mean normal true stress (p) is defined as the average of applied principal stresses, as shown in Eq. (2). Specimen deformations were measured in terms of axial engineering strain (ε_a) and radial engineering strain (ε_r), with volumetric engineering strain (ε_v) defined in Eq. (3). Triaxial confinement pressures of 10 MPa, 50 MPa, 100 MPa, and 200 MPa were selected to facilitate different types of damage modes, i.e., brittle, quasi-brittle, and ductile.

$$q = \sigma_a - \sigma_r \tag{1}$$

$$p = \frac{(\sigma_1 + \sigma_2 + \sigma_3)}{3} = \frac{(\sigma_a + 2\sigma_r)}{3} \tag{2}$$

$$\varepsilon_v = \varepsilon_a + 2\varepsilon_r \tag{3}$$

2.3. X-ray microtomography

For damage visualization and quantification, X-ray microtomography was used for nondestructive characterization. All micro-CT scans presented in this study were conducted on a Bruker Skyscan 1173 high-energy spiral-scan micro-CT with a maximum X-ray energy of 130 kV and a 5-megapixel (2240x2240) flat-panel sensor. Offset scans were used for all specimens by stitching side-by-side horizontal scans for the

purpose of achieving the highest possible resolution. Optimized scan settings for 25.4-mm-diameter concrete specimens were determined to be 130 kV and 60 μA with a rotational step size of 0.20°for 360-degree scans. A 0.25-mm-thick brass filter was also used to remove lower energy X-rays that cause beam hardening artifacts on dense specimens. To reduce the effects of noise in the X-ray detector signal, dark flatfield corrections were updated at 60-minute intervals throughout the scan, and 14 frames were averaged to record each saved X-ray projection image. Random stage movements (up/down) were also employed to reduce any artifacts that might be present from defective pixels in the detector. Voxel sizes were in the range of 8.8–25 μm depending on the specimen size and field of view and are notated in each relevant section. Also note that voxel sizes directly correspond to the separation of each cross-sectional slice as each slice has a thickness of one voxel.

Cone-beam X-ray tomography projection images were reconstructed into cross-sectional images using a Feldkamp algorithm within Bruker's NRecon software paired with the GPUReconServer reconstruction engine [39]. Reconstruction parameters included a beam hardening correction of 15 and a ring artifacts correction of 15. To illustrate the input and output of the reconstruction process, an example projection image and reconstructed cross-sectional image are provided in Fig. 2. Finally, all of the cross-sectional images are vertically stacked to provide a complete dataset made up of 256-bit grayscale spectrum where black voxels represent the lowest density, and white voxels represent the highest density.

The 3D microstructure of each specimen was recorded before and after loading to better understand damage initiation and propagation. Although no microcracking was observed in the concrete matrix of pristine specimens, some microcracks and irregular pores were noted within individual sand particles. Analysis for brittle failure modes focused on isolating large interconnected crack networks for visualization purposes and for measuring shear plane angles. For ductile failure modes (as observed at the macroscale), cracking occurs at a lower length scale that is not detectable within the resolution restrictions of the Skyscan 1173 micro-CT. A ductile failure mode resulting in pore collapse produces many cracks with thicknesses that are below 18 μm, which is equivalent to two pixels for the highest resolution micro-CT scans presented in this study. Nonetheless, micro-CT data still provide a means to quantify changes in pore structure.

2.4. Image segmentation

Reconstructed cross-sectional images were all loaded into DataViewer [39] to manually perform non-deformable dataset registrations of pristine and damaged datasets to have the same orientation using sagittal, coronal, and transverse plane views as shown in Fig. 3. Subsequently, unique features at the top and bottom boundaries of the pristine volumes of interest (VOIs) were identified in the damaged specimen scan data to appropriately determine the orientation and upper/lower bounds for damaged VOIs. After registration, binary image operations were performed in CT-Analyzer [39]. Segmentation began with an automatic Otsu threshold method applied to a global histogram function while visually confirming that pore space was segmented appropriately from the surrounding concrete matrix. After segmenting distinct phases, the region of interest (ROI) shrink-wrap tool from CT-Analyzer [39] was implemented to define the region of interest. Analysis included 2D measurements for the porosity of individual cross-sectional images and 3D measurements for global porosity measurements. Furthermore, individual object analysis was performed on each and every discreet binarized object, i.e., pore, in terms of either volume equivalent sphere diameter or major diameter. Objects were also binned into color coded images based on pore sizes to produce 3D images that clearly compare and contrast void structures before and after triaxial loading.

The geometry of brittle damage observed in the specimens features multiple hairline fractures that are poorly captured by the thresholding segmentation. The fractures are segmented with discontinuities or not identified at all. Similarly, the fine aggregate posed problems with thresholding due to either thin features (shells) or high local variations of intensity (larger objects). Thus, to observe how fracture patterns relate to all phases in the material, selected specimens have been segmented with a manually trained Fast Random Forest machine learning algorithm [40–41]. After segmentation, fracture geometry has been inspected and corrected manually to provide the most accurate representation.

3. Results and discussion

3.1. Triaxial compression data

Triaxial compression (TXC) specimens were tested with length-to-diameter ratios (L/D) of 2.0 (25 mm ×50 mm) and 1.0 (25 mm ×25 mm). Replicate tests were conducted at each combination of pressure level and specimen size. For the first phase of a triaxial experiment, the specimen is initially loaded hydrostatically up to the desired confinement pressure. To illustrate material behavior under hydrostatic compression (HC) conditions, Fig. 4 presents loading and unloading data for hydrostatic specimens up to a mean normal stress (p) of 200 MPa. Note that the hydrostatic loading is fully reversible under these test conditions, i.e., no observable macroscale plasticity. TXC data are presented in Fig. 5 and Fig. 6, where each curve represents the average of two replicate experiments. Results are plotted in terms of both

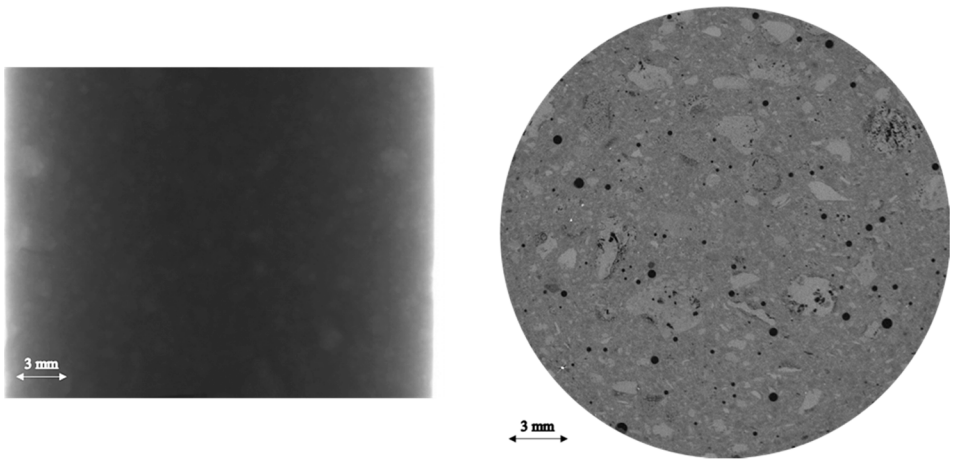

Fig. 2. X-ray projection image (left) and reconstructed cross-sectional image (right).

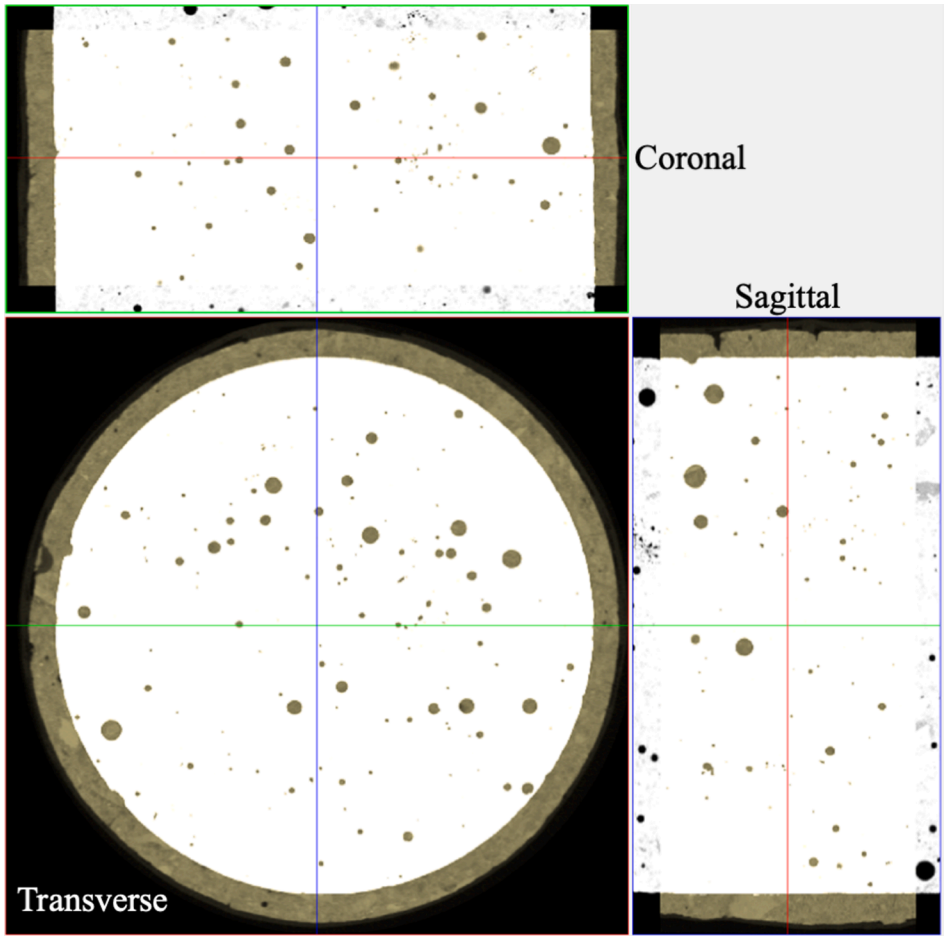

Fig. 3. DataViewer registration example for pristine (white) and damaged (brown) micro-CT scan data.

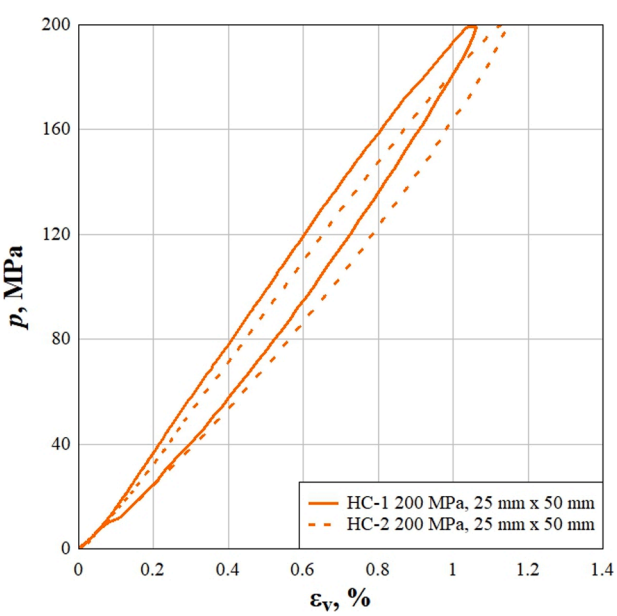

Fig. 4. Hydrostatic loading and unloading for 25 mm ×50 mm specimens up to 200 MPa mean normal stress.

volumetric strains and axial strains. Although axial strains have been reported and discussed previously [38], the inclusion of volumetric strain measurements provides valuable insight when interpreting micro-CT imagery of triaxially damaged specimens.

For all data presented in this paper, compression is considered positive. Therefore, axial strains are reported as positive while the specimen length decreases. Similarly, a positive volumetric strain indicates a decrease in the volume of the specimen. However, note that volumetric strains are calculated based on a combination of axial and radial strain measurements. As the concrete specimen begins to fail, internal crack formation causes expansion and a measured increase in volume.

Considering Figs. 5, 10 MPa TXC experiments with an L/D of 2.0 exhibit an extremely brittle failure mode that is typical for unconfined compression experiments. However, the corresponding specimens with an L/D of 1.0 experience a higher peak stress with volumetric strains decreasing near failure indicating that damage accumulation is likely more substantial as compared to the taller specimens. For the 50 MPa TXC experiments, specimens were unloaded shortly after reaching a peak stress, and the recovered specimens were mostly intact with some fragmentation observed. The 50 MPa TXC data for specimens having an L/D of 1.0 exhibited a larger decrease in volumetric strains after reaching a peak volumetric strain that is likely attributed to increased damage accumulation as compared to L/D = 2 specimens. The noted discrepancies from size effects are likely a result of higher confinement stresses in the shorter specimens due to end effects where frictional confinement accumulates along specimen-platen interface.

At higher confinement pressures presented in Fig. 6, specimen size continues to have substantial effects on material behavior. For 100 MPa and 200 MPa TXC experiments, the tests are stopped after reaching an axial strain of 15% for the purpose of directly comparing material behavior. Note that these specimens experience a ductile failure mode and continue to have substantial load bearing capacity at axial strains

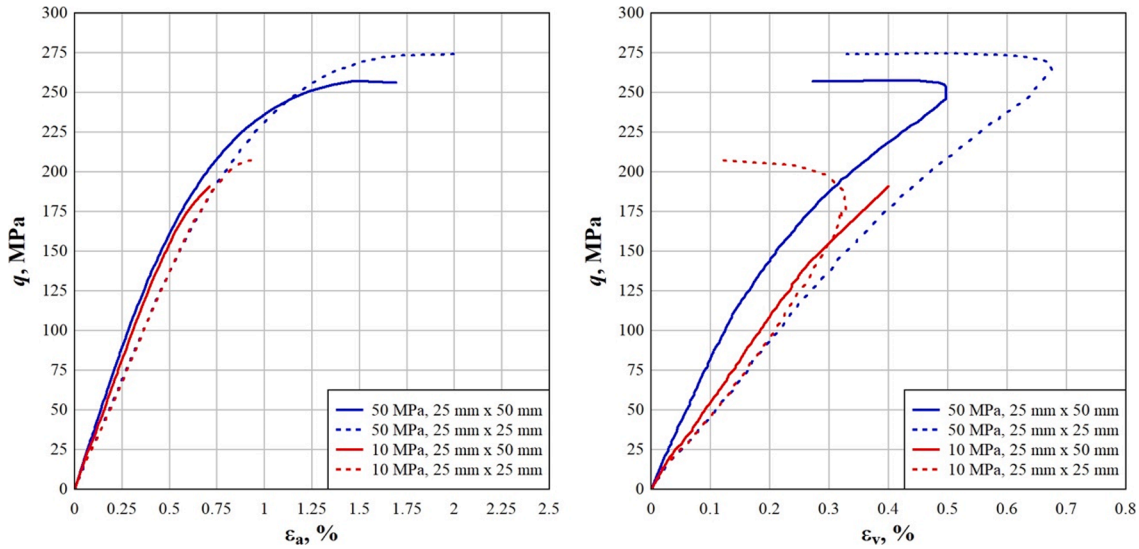

Fig. 5. Material response in terms of axial (left) and volumetric (right) strains for 25 mm ×50 mm and 25 mm ×25 mm TXC specimens at 10 and 50 MPa confining pressure.

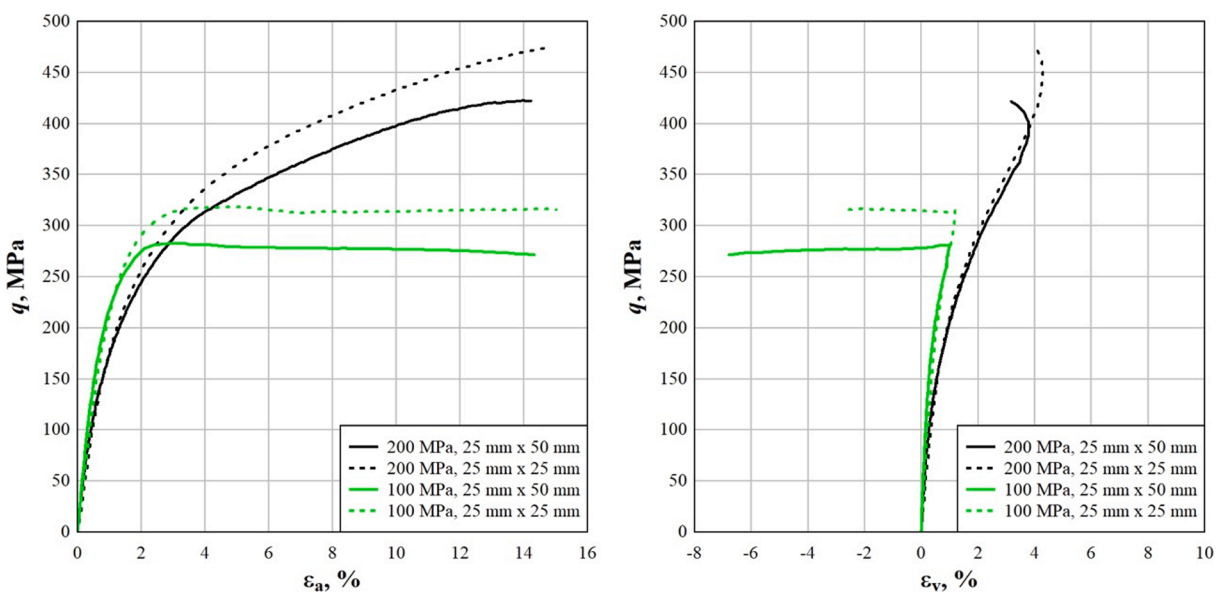

Fig. 6. Material response in terms of axial (left) and volumetric (right) strains for 25 mm ×50 mm and 25 mm ×25 mm TXC specimens at 100 and 200 MPa.

beyond 15%. Prior to reaching a peak volumetric strain, changes in L/D do not appear to have any effect on volumetric response. As discussed further in sections 3.3 through 3.5, gauge-indicated volumetric strain readings are not reliable when the volumetric strains begin to move in the negative direction. However, in a relative sense, the amount of negative volumetric strain indicates the severity of non-uniform specimen deformation where the central region of the specimen expands more than the specimen ends (also referred to as barreling).

3.2. Limitations of volumetric strain measurements

Volumetric strain measurements have limited use when approaching peak stress values since specimen cross-section is not uniform throughout the vertical axis after undergoing large axial deformations. To clearly observe non-uniform deformations, four specimens were tested to axial strains of ~30%. The material responses are plotted in Fig. 7 with volumetric strains plotted based on gauge-indicated values for ε_a and ε_r and the use of Eq. (3). However, this method for calculating volumetric strain is only valid if deformations are uniform throughout the vertical axis of the specimen since the radial strain is only determined at one location in the center of the specimen. To better understand the deficiencies of in situ volumetric strain calculations, posttest gauge-indicated readings were compared to posttest micro-CT-indicated volume measurements from the full specimen volume as shown in Table 2. As mentioned earlier, a positive volumetric strain represents a reduction in volume, thus a negative volumetric strain should represent an increase in volume.

The large negative values for volumetric strains are clearly errant as triaxial compression does not lead to expansion within the concrete microstructure. Referencing the gauge-indicated and micro-CT indicated volumetric strain measurements in Table 2, note that after unloading, gauge-indicated volumetric strains differ from micro-CT results by 10–30%. This error can be attributed to the fact that the deformation-based radial engineering strain calculation only utilizes a single centrally located measurement that cannot account for non-uniform deformation. Therefore, the gauge-indicated volumetric

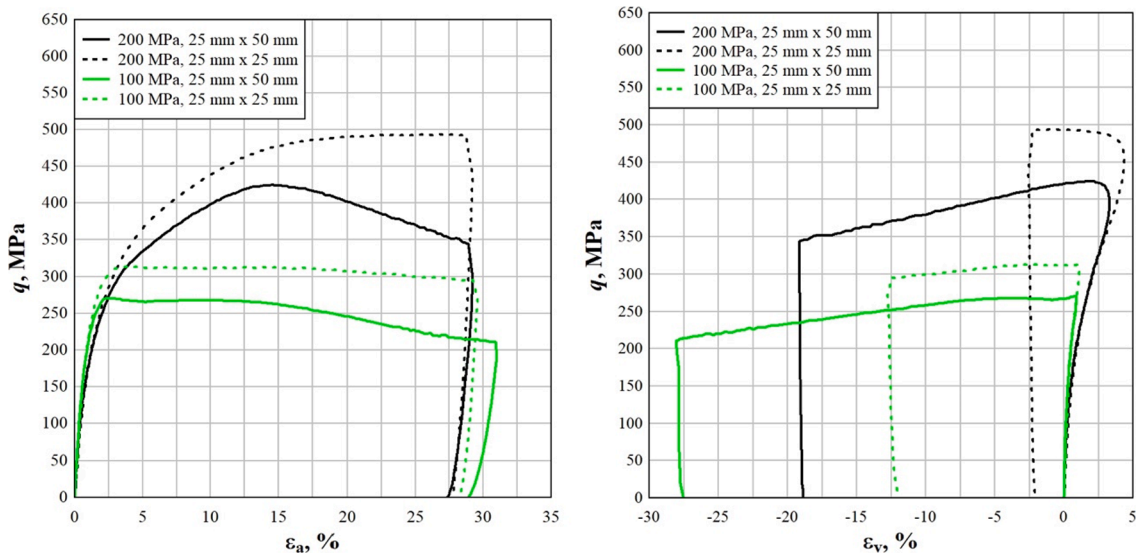

Fig. 7. Gauge indicated material response in terms of axial (left) and volumetric (right) strains for large deformations ($\varepsilon_a \cong 30\%$).

Table 2
Volumetric strain readings from in situ gauges and ex situ micro-CT measurements for specimens loaded to $\varepsilon_a \cong 30\%$.

Specimen	Gauge indicated ε_v (%)	Micro-CT indicated ε_v (%)
100 MPa, L/D = 2.0	−27.6	2.12
100 MPa, L/D = 1.0	−12.0	1.73
200 MPa, L/D = 2.0	−18.8	5.71
200 MPa, L/D = 1.0	−2.1	7.91

readings should be neglected at the onset of non-uniform specimen deformation where calculated volumetric strains begin to move in the negative direction. Although large deformation volumetric strain readings can be misleading due to non-uniform specimen geometry, high axial strains were required to reach a true peak stress for the 200 MPa TXC specimens with L/D = 1.0. In cases where non-uniform specimen deformation is anticipated, additional in-situ measurement locations would provide a more accurate estimate of volumetric strain history. Micro-CT provides an additional method to verify specimen volume measurements before and after loading.

3.3. Visual observations from micro-CT

For preliminary observations, full-specimen micro-CT scans were conducted on all damaged specimens using voxel sizes of 25 μm or 18 μm for specimens with a height of 50 mm or 25 mm, respectively. Prior to looking at triaxially damaged specimens, we will first observe fracture patterns in unconfined compression experiments to provide a baseline reference. For high-strength concretes, a common failure mode in unconfined compression (especially with lubricated surfaces to reduce end friction) is actually a tensile driven failure mode known as axial splitting [42–43]. The vertical cracking failure mode is defined as a Type III fracture by ASTM C39 [44]. For BBR9 specimens tested in uniaxial compression with MoS_2 lubricant applied to the specimen/platen interface, most specimens failed with a Type III columnar fracture pattern as shown in Fig. 8. Although less common, damage modes similar to Type II (well-formed cone on one end with vertical cracks) and Type IV (diagonal cracking) fracture patterns were observed in some cases. These specimens were preserved for micro-CT analysis by using a flexible latex membrane to contain post-fracture rubblized concrete debris.

All specimens exposed to multi-axial stress states were isolated from the hydraulic fluid using a latex membrane that was removed prior to

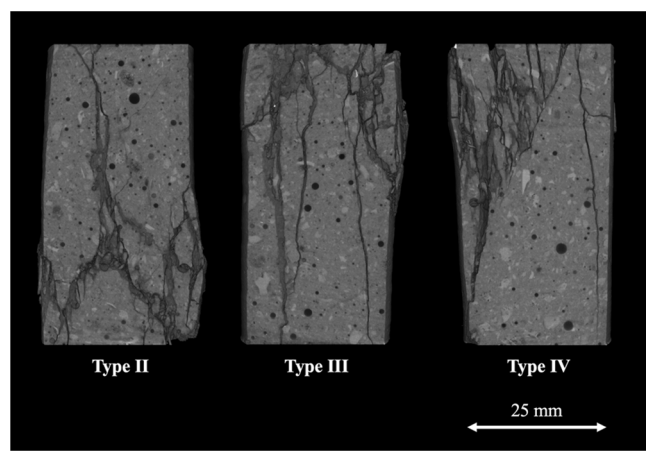

Fig. 8. Micro-CT imagery of concrete fracture patterns under unconfined compression.

micro-CT analysis. Images of damaged concrete specimens from hydrostatic and triaxial loadings up to 200 MPa are presented in Fig. 9. Note that after a 200-MPa hydrostatic compression (HC) experiment, the specimen still appears to be in a pristine condition. It is interesting to note that visually observable damage is minimal even at high hydrostatic pressure, as expected based on the data recorded in Fig. 4. As the shear component is introduced during triaxial compression (TXC) experiments, damage progresses through different failure modes. TXC specimens undergoing a brittle failure mode, i.e., 10 MPa and 50 MPa experiments, were unloaded after reaching a peak, whereas TXC specimens undergoing a ductile failure mode, i.e., 100 MPa and 200 MPa, were unloaded after reaching an axial strain of 15%. At 10 MPa, the concrete undergoes a brittle failure mode similar to that of the unconfined specimens. However, this low level of confinement pressure changes the fracture pattern from axial splitting to a dominant shear fracture. For the 50-MPa triaxial test, the concrete specimen still exhibits a primarily brittle (or quasi-brittle) failure mode. In this case, quasi-plastic deformations allow damage to accumulate throughout the specimen as it undergoes slightly higher axial strains as compared to 10-MPa TXC experiments. For 100-MPa TXC experiments, the concrete displays a clear transition from brittle to ductile failure. Plastic deformations result in a failure mode where porosity collapses/crushes. A slight barreling shape is also observed, which is likely attributed to

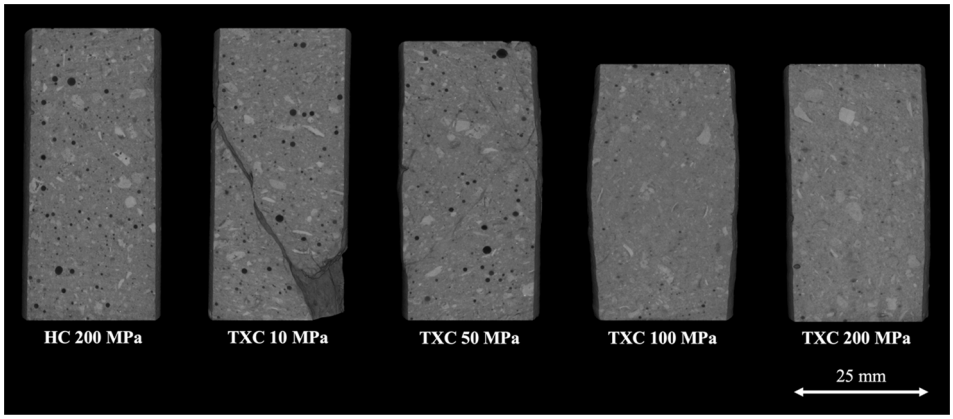

Fig. 9. Micro-CT imagery of damaged concrete after multi-axial loading.

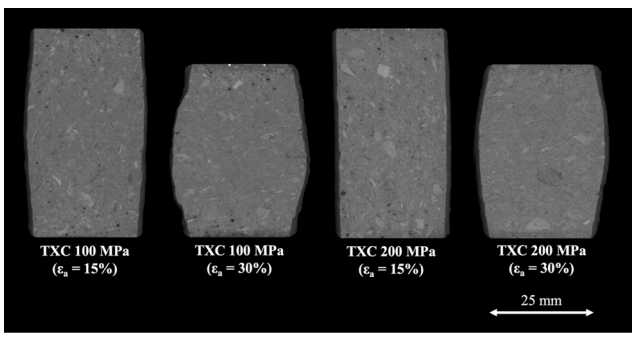

Fig. 10. Comparison of damaged geometry at high confinement pressures with increasing axial deformations.

additional confinement caused by end effects. Lastly, the 200-MPa triaxial specimens exhibit a failure mode that is similar to 100-MPa TXC specimens. However, at this maximum pressure, cracks are not discernable in the micro-CT images, and end effects become less substantial as the specimen undergoes uniform deformation in the radial direction. Visual observations show that barreling is more pronounced in 100-MPa TXC specimens as compared to 200-MPa TXC specimens, which was predicted by the volumetric strain behavior as discussed at the end of section **3.1**.

Historically, triaxial experiments conducted at the U.S. Army Engineer Research and Development Center (ERDC) triaxial testing facility have only gone up to axial strains of 15%. In prior work, it was predicted that non-uniform deformation becomes dominant at axial strains beyond this point [38]. To further verify this claim, 100-MPa and 200-MPa TXC experiments were conducted to axial strains of ~30% to confirm deformed specimen geometries. As shown in Fig. 10, barreling becomes much more pronounced at higher axial strains, and volumetric strain calculations based on uniform radial deformations are no longer valid as previously discussed in section **3.2**.

Finally, damage modes were also observed for specimens with a reduced length-to-diameter ratio (L/D). The 25-mm ×25-mm specimens

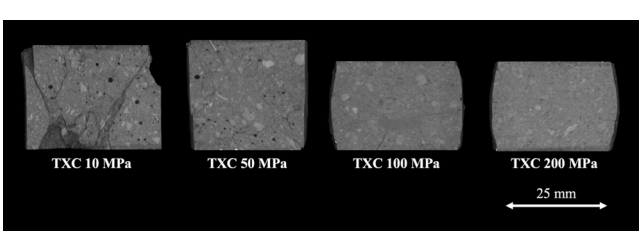

Fig. 11. Micro-CT imagery of TXC specimens with L/D = 1.0.

(L/D = 1.0) shown in Fig. 11 were exposed to the same testing conditions as the 25-mm ×50-mm (L/D = 2.0) TXC specimens from Fig. 9 (ε_a = 15% for TXC specimens at 100 MPa and 200 MPa). As noted in section 3.1, there is an observed strength increase when transitioning from L/D = 2 to L/D = 1 that is likely due to end effects. Furthermore, fracture patterns also change with variations in L/D. For the 10-MPa TXC experiments, the shorter specimen is able to endure multiple shear cracks rather than a single, dominant failure plane. The 50-MPa TXC specimen appears to have a higher degree of crack saturation as compared to the taller specimen geometry. At 100 MPa, the L/D = 1.0 specimen shows visible cracks near the specimen's ends that were not apparent at L/D = 2.0. However, no visible cracks are observed at 200 MPa in either specimen geometry. Damage isolation and quantification is further evaluated in sections 3.4 and 3.5.

3.4. Isolation of crack patterns for brittle failure modes

As confinement pressure increases, material response transitions from a brittle failure mode to a ductile failure mode. However, even within the brittle failure mode, damage morphology and crack saturation can vary widely. To confirm visual observations, the scan data detailed in section 3.3 were used to isolate 3D damage in full specimens. In Fig. 12 and Fig. 13, full specimen scans are presented for 10-MPa and 50-MPa TXC tests, respectively. Although macrocracks are clearly seen, microcracks connect with nearby pores and are not clearly resolved. Therefore, additional scans were conducted on a centrally located volume of interest (VOI) to maximize resolution (8.8 μm voxel size) while capturing the full specimen diameter. The reduced VOIs were then carefully segmented in 2D and 3D to visualize microcracking. The high-resolution scans intentionally remove connected pores to more clearly visualize crack morphology.

For 10 MPa TXC experiments, shear dominated the fracture pattern. As observed in Fig. 12, the 25-mm ×50-mm (L/D = 2.0) specimen failed through a primary crack at an angle of ~30° from the vertical axis with a clearly defined shear plane. In contrast, the 25-mm ×25-mm (L/D = 1.0) specimen shown in Fig. 12 has multiple shear planes with crack angles ranging from 25 to 30° from the vertical axis. The high-resolution scan was used to produce phase-segmented 2D images from the 10-MPa TXC high-resolution scans as presented in Fig. 14, Although the L/D = 1.0 specimen displays local damage, the L/D = 2.0 specimen reveals distributed microcracking with high concentrations surrounding primary failure planes.

As the confinement pressure increases to 50 MPa, observable damage progression continues to occur primarily through brittle fracture planes. In Fig. 13, the 25-mm ×50-mm (L/D = 2.0) specimen shows two intersecting shear planes at angles ranging from 25° to 30° from the vertical axis. Also in Fig. 13, the 25-mm ×25-mm (L/D = 1.0) specimen shows similar shear-cracking angles with distributed shear planes

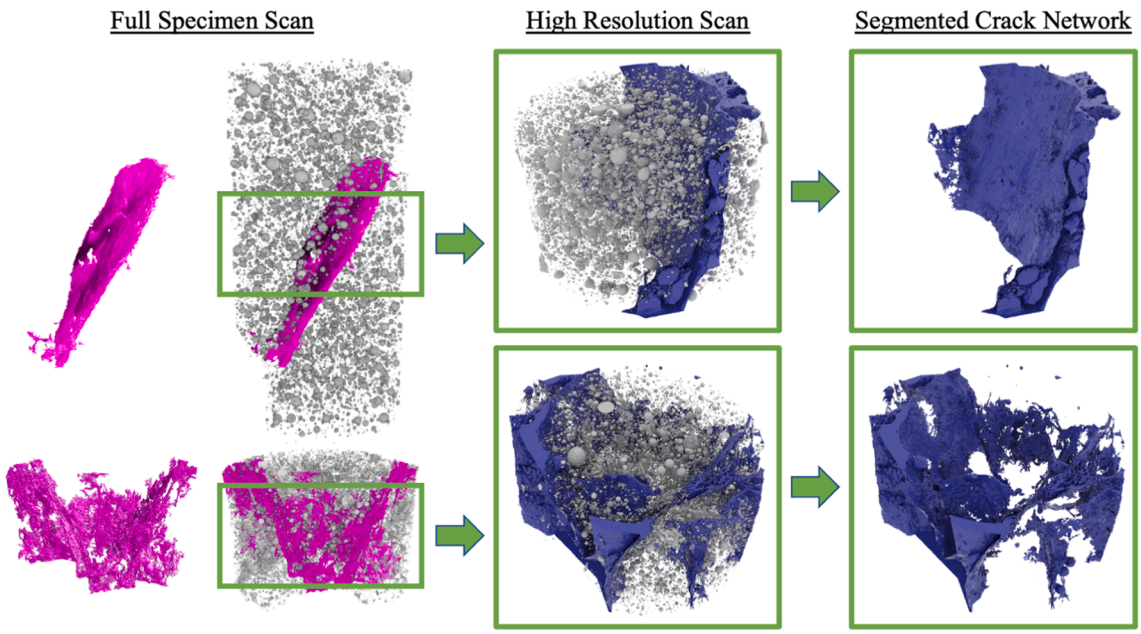

Fig. 12. Crack segmentation for 10 MPa TXC specimens withL/D = 2.0 (top) and L/D = 1.0 (bottom).

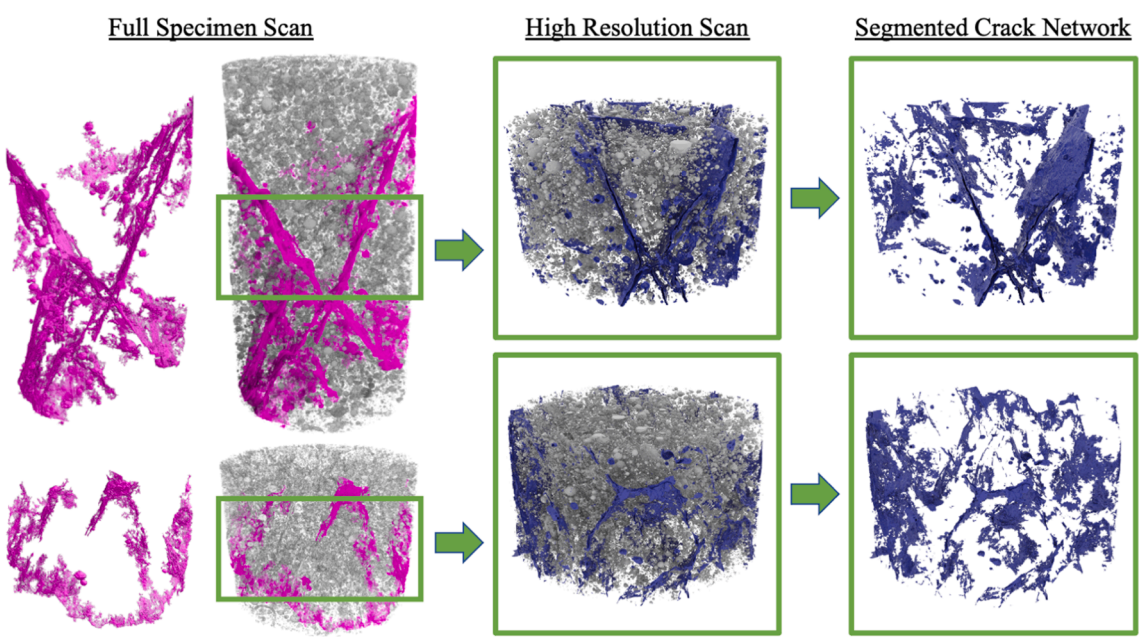

Fig. 13. Crack segmentation for 50 MPa TXC specimens with L/D = 2.0 (top) and L/D = 1.0 (bottom).

throughout the specimen. In both specimen geometries, coalescence of microcrack networks and large voids ultimately leads to brittle failure (as seen in the full specimen segmented damage in Fig. 12 and Fig. 13. Taking a closer look at microstructure in Fig. 15, it is evident that microcracks are present throughout the specimens for both geometries. It is important to keep in mind that as crack widths become smaller, damage is more difficult to segment due to the resolution limitations of the micro-CT scanner.

When comparing damage from unconfined compression (Fig. 8, 10-MPa TXC and 50-MPa TXC specimens, a stark contrast in crack patterns is observed. Although axial splitting is the primary failure mode in unconfined compression experiments, failure occurs along shear planes in triaxial experiments at confining pressures of 10 MPa and 50 MPa. As confinement pressure increases, damage modes transition towards plastic deformation. This is further supported by the higher number of shear crack planes observed with reduced L/D specimens that undergo additional confinement as a result of frictional end effects. Shear-plane angles remain consistently in the range of 25° to 30° from the vertical axis for both specimen geometries at confining pressures of 10 MPa and 50 MPa.

3.5. *Quantifying damage for ductile failure modes*

At higher confinement pressures, brittle failure modes are absent from the CT images of the deformed specimens. Instead, large axial deformation (high ductility) accompanied by significant reduction in porosity becomes prevalent, which is a hallmark for ductile failure of concrete [45]. All porosity analyses used maximum resolution (8.8-μm

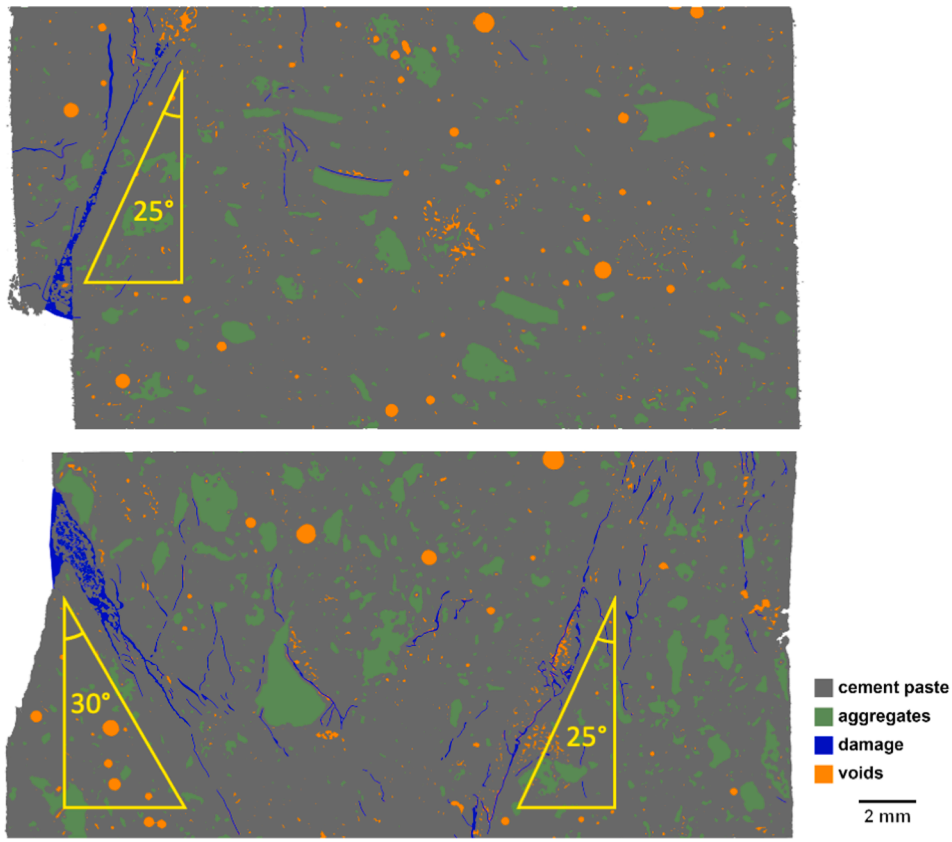

Fig. 14. Fracture patterns for 10-MPa TXC specimens with L/D = 2.0 (top) and L/D = 1.0 (bottom).

voxel size) scans to capture pore sizes distributions. In this case, the scans focused only on the central portion of the specimen with a volume of interest (VOI) height of 14.3 mm. To visualize local variations and changes in pore structure, porosity was calculated for each cross-sectional image throughout the vertical axis of the VOI. This 2D investigation provides evidence that both pristine porosity and damaged porosity is well-distributed, thus indicating that the specimens are representative of the bulk material response. Furthermore, a 2D investigation presents a unique perspective in considering the evolution of local pore sizes. Since the length of a specimen changes during testing, results are presented in terms of normalized axial position where "0″ represents the bottom of the VOI and "1" represents the top of the VOI. Fig. 16 presents local porosity variations for 100-MPa and 200-MPa TXC specimens after undergoing axial strains of ~15% (left) and ~30% (right).

The variability in local porosity values for pristine specimens is an indication of the heterogeneous nature of concrete, yet there is no localization of pore collapse. Although cross-sectional values of porosity in pristine BBR9 specimens ranged from 1 to 5%, the mean total porosity was determined to be 3.01% (not accounting for porosity with a volume-equivalent sphere diameter below 50 μm). Referencing Fig. 16, no substantial differences were observed in terms of L/D. Specimens undergoing 15% axial strains in 100-MPa and 200-MPa TXC experiments did not show any clear discrepancies in terms of cross-sectional porosity measurements with mean values of 0.25% and 0.29%, respectively. However, at axial strains of 30%, mean porosity values were 0.14% for 100-MPa TXC specimens as compared to 0.03% for 200-MPa TXC specimens, indicating that pores are more thoroughly collapsed under higher pressure.

In a separate investigation, a 3D individual object analysis was conducted on each pore within the VOI to develop porosity size distributions in terms of volume-equivalent sphere (VES) diameters ranging from 45 μm up to 4 mm. Bin sizes started at a minimum of 45 μm to ensure that a sufficient number of voxels (8.8 μm) were used to resolve individual pore morphologies. Starting with the smallest bin size, each subsequent bin size was identified using a multiplier of 1.1 until reaching a maximum bin size of 3.64 mm. For example, the first bin counts pores with VES diameters from 45 μm up to 50 μm, the second bin would cover VES diameters above 50 μm up to 55 μm, i.e., 50 μm multiplied by 1.1, the third bin would cover VES diameters above 55 μm up to 60.5 μm, i.e., 55 μm multiplied by 1.1, and so forth. The resulting pore size distributions were then plotted in a log-log format as shown in Fig. 17 to clearly visualize distribution data for the full range of pore sizes. Also note that the total number of pores decreases after TXC testing since VES diameters below 45 μm cannot be accurately measured using the micro-CT technique.

Pore size distributions for pristine specimens were observed to be quite consistent considering the heterogeneous nature of concrete. Similar to observations made for Fig. 16, the pore size distributions are quite similar for all damaged specimens undergoing axial strains of ~15%. However, it does appear that the 200 MPa TXC tests provided slightly more compaction for damaged volume-equivalent sphere diameters ranging from 50 to 120 μm. Also following observations from Fig. 16, samples undergoing axial strains of ~30% had more severe pore collapse (for all damaged pore sizes) in 200 MPa TXC specimens as compared to 100 MPa TXC specimens. As barreling becomes more pronounced at high axial strains, 100 MPa TXC specimens exhibit relatively larger radial deformations while the higher confinement in 200 MPa TXC specimens continues to drive the additional compaction of remaining void structures. Although reducing L/D has been shown to increase peak stress values, changes in L/D do not show substantial differences for ductile failure modes.

Since L/D was determined to have negligible effects on pore size distributions, visualization efforts were solely focused on specimens with a traditional L/D of 2.0. Each image in Fig. 18 and Fig. 19 depict a specimen with pristine porosity shown on the left half and damaged

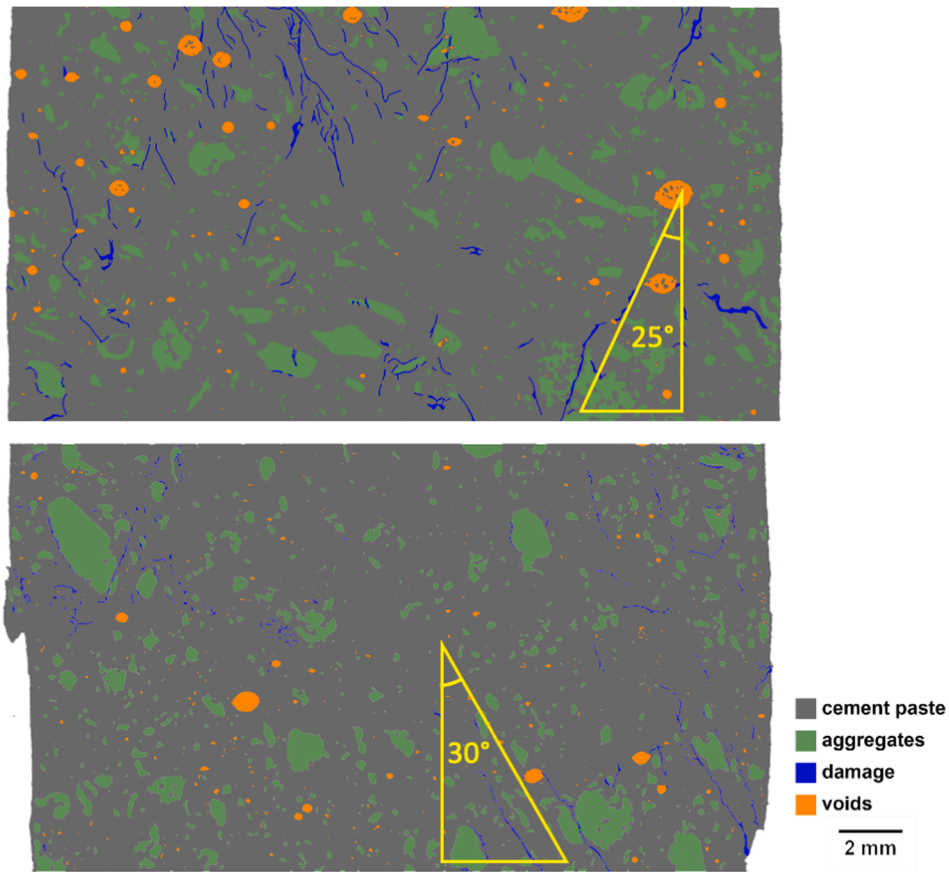

Fig. 15. Fracture patterns for 50-MPa TXC specimens with L/D = 2.0 (top) and L/D = 1.0 (bottom).

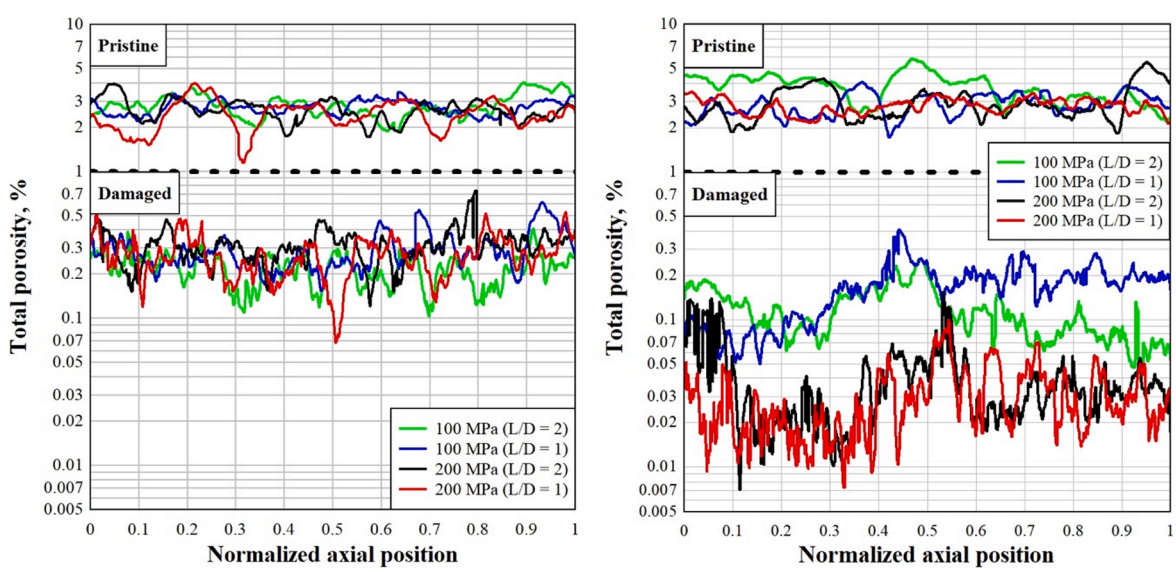

Fig. 16. Cross-sectional porosity percentages for 2D sections in terms of normalized axial position before and after ~15% (left) and ~30% (right) axial strain deformations.

porosity shown on the right half for a given VOI. Pores are color coded by major diameter to conveniently distinguish individual pores and sizes.

In pristine specimens, porosity is nearly spherical resulting in a major diameter that is approximately equivalent to the volume-equivalent sphere diameters presented in Fig. 17. However, damaged pores are more clearly distinguished by major diameter since the pore geometry is severely flattened after axial loading. The 3D rendering of damaged pore structures in Fig. 18 reveals similar void structures for 100-MPa and 200-MPa TXC specimens undergoing axial strains of ~15%. However, discrepancies are observed after ~30% axial strain deformations in Fig. 19 with the 200-MPa TXC specimen having a smaller number of observable pores as compared to the 100-MPa TXC specimen. As expected, the damaged VOI (adapted to contain the same pores/features as

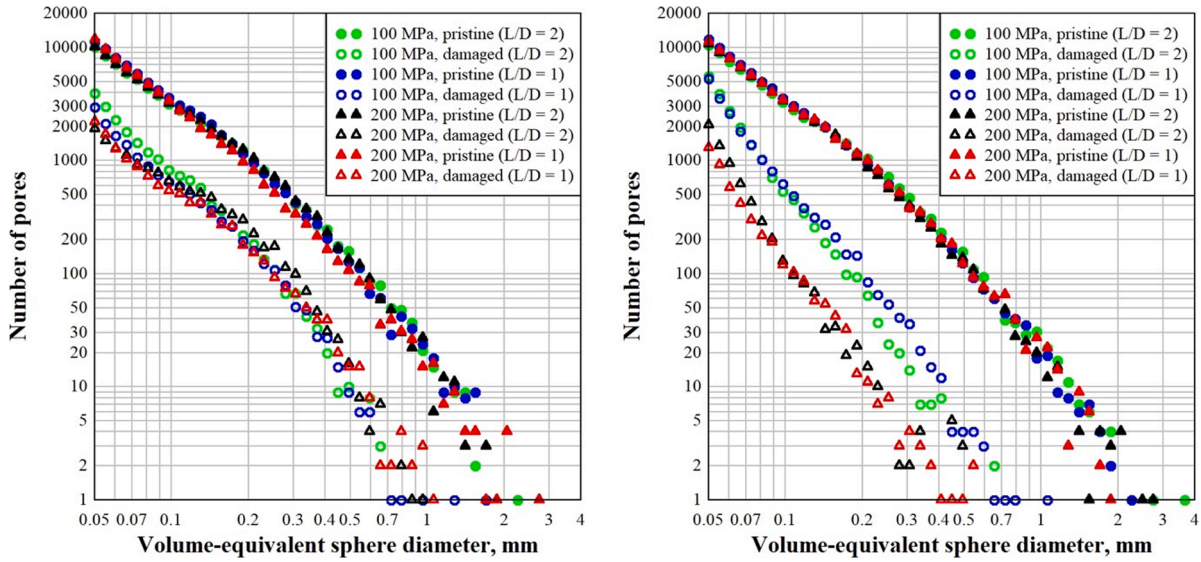

Fig. 17. Void analysis in terms of volume-equivalent sphere diameter before and after ~15% (left) and ~30% (right) axial strain deformations.

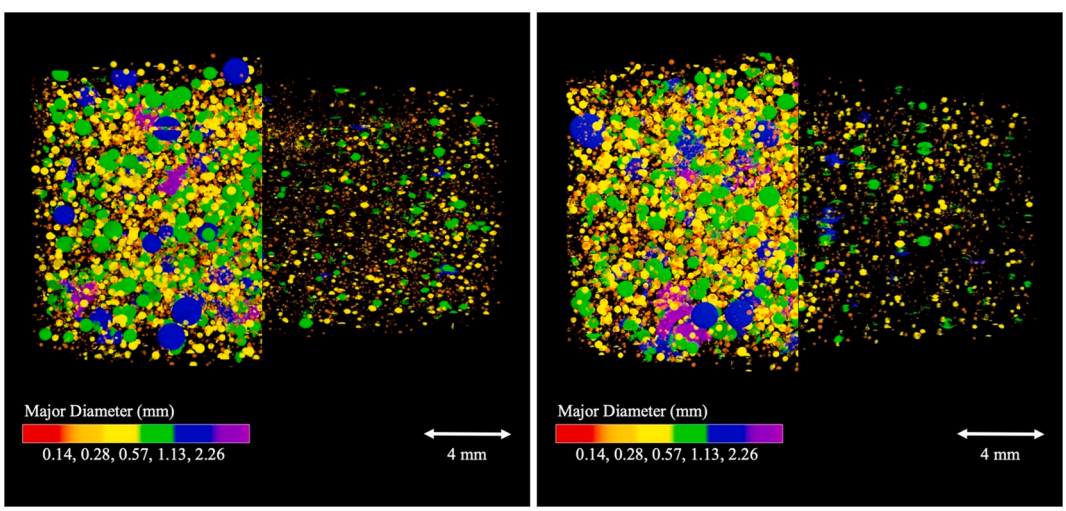

Fig. 18. Void structure for pristine and damaged 100 MPa (left) and 200 MPa (right) TXC specimens after ~15% axial strain deformations.

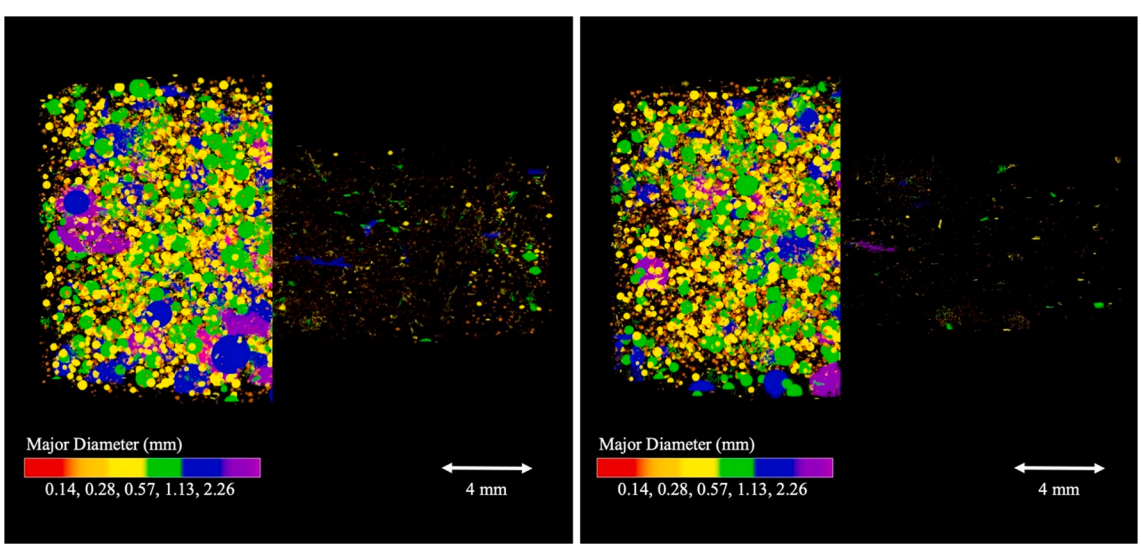

Fig. 19. Void structure for pristine and damaged 100 MPa (left) and 200 MPa (right) TXC specimens after ~30% axial strain deformations.

the pristine VOI) shrinks in height and expands radially as compared to the pristine VOI. The qualitative pore structure images in Fig. 18 and Fig. 19 provide visual evidence that is consistent with quantitative porosity measurements presented earlier in Fig. 16 and Fig. 17.

3.6. Residual strength measurements

Residual strength experiments were conducted to provide a means for correlating pore collapse (as presented in section 3.5) to a physical measurement of strength degradation resulting from microstructural damage. Residual strength measurements were obtained for all triaxially damaged 100 MPa and 200 MPa TXC specimens by performing destructive unconfined compression experiments. As a reference for comparison, the mean unconfined compressive strength of pristine BBR9 specimens with LD = 1 and L/D = 2 was previously reported to be 140.7 MPa and 130.8 MPa, respectively [38]. Residual strength measurements for damaged specimens are reported in Table 3. Stress measurements were calculated by using the largest specimen diameter in the center of each triaxially damaged specimen. The residual strengths presented here represent the most conservative value since significant central bulge may underestimate stresses with cross-sectional area measurements varying by up to 35% within an individual damaged specimen. Residual strength percentages were calculated by dividing the residual strength by the mean strength for pristine specimens having the same L/D.

After undergoing axial strains of ~15%, 100-MPa and 200-MPa TXC specimens retain approximately 40% and 50%, respectively, of their pristine strength capacity. Even after undergoing axial strains of ~30%, 100-MPa and 200-MPa TXC specimens retain approximately 30% of their pristine strength capacity. The substantial losses in load-bearing capacity are likely due to microcracking at a length scale that is not detectable using micro-CT. However, the residual strength measurements indicate that the cohesive strength of TXC specimens undergoing a ductile failure mode remains substantial and should be considered when defining a damage variable.

4. Conclusions

X-ray microtomography was used to analyze both pristine and damaged high-strength concrete specimens to characterize damage modes and size effects under hydrostatic and triaxial stress states. Specimens with a diameter of 25 mm and an L/D of either 1 or 2 were evaluated to determine damage features under triaxial confinement pressures of 0, 10, 50, 100 and 200 MPa. The conclusions below are based on the findings of this research.

- Axial splitting is the dominant failure mode for BBR9 high-strength concrete specimens under unconfined compression.
- Deformations at hydrostatic pressures up to 200 MPa are fully reversible. Although the confining pressure is significant, a shear component is required to initiate plastic deformation. This indicates that the elastic limit in a corresponding material model should be at least 200 MPa.

Table 3
Residual strength measurements.

Confining Pressure, MPa	Axial Strain, %	Length-to-diameter ratio (L/D)	Residual Strength, MPa	Residual Strength, %
100	~15	1	49.9	35.5
100	~15	2	56.1	42.9
100	~30	1	47.7	33.9
100	~30	2	31.8	24.3
200	~15	1	67.7	48.1
200	~15	2	69.9	53.4
200	~30	1	48.9	34.8
200	~30	2	40.8	31.2

- Volumetric strain measurements can be recorded using a centrally located LVDT-based lateral deformeter, noting that signals are only valid up to the point where volumetric strains turn negative due to non-uniform specimen deformation. Removable gauge mounts are critical for conducting micro-CT scans on damaged triaxial specimens.
- Micro-CT provides an accurate approach for measuring ultimate volumetric strains for irregularly shaped damaged specimens.
- From visual observations based on two experiments at each testing condition, a transition in damage mode is noted as confining pressure increases, e.g., at 10 MPa, brittle failure through a single crack with a predominant shear failure, at 50 MPa, quasi-brittle failure with distributed microcracks ultimately leading to shear failure, at 100 MPa, ductile failure with minimal observable microcracks and damage primarily consisting of pore collapse, and at 200 MPa, ductile failure with no discernable cracking and damage observed through pore collapse and crushing.
- At axial strains of 30%, specimen geometry presents a severe barreling shape leading to substantial variations in cross-sectional area throughout the specimen. However, at axial strains of 15%, the observed variations in cross-sectional area are minimal.
- Brittle and quasi-brittle fracture modes for 10–50 MPa TXC experiments presented shear planes at angles ranging 25° to 30° from the vertical axis.
- As specimens undergo triaxial compression at 100–200 MPa, spherical voids are flattened into ellipsoidal morphologies as total porosity percentages continue to reduce.
- After undergoing 15% axial strains, individual object analysis shows that specimens damaged under 200-MPa TXC include a more noticeable reduction of pore sizes in the range of 50–120 μm as compared to 100-MPa TXC specimens.
- After undergoing 30% axial strains, porosity-size distributions are noticeably lower for all pore sizes undergoing 200-MPa TXC as compared to 100-MPa TXC. This observation can be explained by the fact that the 200-MPa TXC specimens undergo a more complete pore collapse with smaller radial strain measurements for a given axial deformation as compared to the 100-MPa TXC specimens.
- After undergoing axial strains of ~15–30%, triaxially damaged specimens in a ductile failure mode maintain a residual unconfined compressive strength that is ~30–50% of the pristine strength.

For axial strains up to 15%, the damage modes under the same confining pressure were very similar regardless of the change in length-to-diameter ratio (L/D). This observation indicates that specimens with a reduced L/D could be reasonably used to assess mechanical properties for high-strength concrete, although perceived strength increases as a result of end effects should still be considered. Based on the similarities in damage modes with varied specimen lengths, L/D = 1 specimens should be suitable for experimental methods using a triaxial Kolsky bar where the specimen length must be restricted to ensure a constant strain rate deformation under dynamic stress equilibrium. Additionally, the unique damage observations from this study are being used to inform microstructural failure simulations. Since substantial reduction was observed on the residual strength of TXC specimens with no demonstration of apparent macroscopic failure, future work should explore alternate techniques for observing and quantifying damage at lower length scales.

CRediT authorship contribution statement

Brett Williams: Investigation, Formal analysis, Visualization, Writing – original draft. **Anna Madra:** Formal analysis, Visualization, Writing – original draft. **William Heard:** Conceptualization, Supervision. **Steven Graham:** Methodology. **Michael Grotke:** Methodology. **Michael Hillman:** Supervision, Writing – review & editing. **Xu Nie:** Writing – review & editing.

Declaration of Competing Interest

The authors declare that they have no known competing financial interests or personal relationships that could have appeared to influence the work reported in this paper.

Acknowledgement

We thank the following ERDC personnel for their contributions to this research, i.e., Robert Moser and Jesse Sherburn for assistance in proposal development, Kerry Ratliff for support in triaxial testing, Jason Morson and Terry Smith for their assistance with specimen preparation, and Mickey Blackmon and Christopher Ables for machining components to conduct triaxial experiments. We also thank Bradley Martin from the Air Force Life Cycle Management Center for assistance in proposal development.

The use of trade, product, or firm names in this document is for descriptive purposes only and does not imply endorsement by the U.S. Government. The tests described and the resulting data presented herein, unless otherwise noted, are based on work conducted by the U.S. Army ERDC. Permission was granted by the Director, Geotechnical and Structures Laboratory to publish this information. The findings of this report are not to be construed as an official Department of the Army position unless so designated by other authorized documents.

References

[1] H. Toda, I. Sinclair, J.Y. Buffiere, E. Maire, K.H. Khor, A 3D measurement procedure for internal local crack driving forces via synchrotron X-ray microtomography, Acta Materialia (2004), https://doi.org/10.1016/j.actamat.2003.11.014.

[2] E.N. Landis, T. Zhang, E.N. Nagy, G. Nagy, W.R. Franklin, Cracking, damage and fracture in four dimensions, Mater Struct 40 (4) (2007) 357–364, https://doi.org/10.1617/s11527-006-9145-5.

[3] S. Huang, K. Xia, H. Zheng, Observation of microscopic damage accumulation in brittle solids subjected to dynamic compressive loading, Review of Scientific Instruments 84 (9) (2013) 093903, https://doi.org/10.1063/1.4821497.

[4] S.C. de Wolski, J.E. Bolander, E.N. Landis, An in-situ x-ray microtomography study of split cylinder fracture in cement-based materials, Exp Mech 54 (7) (2014) 1227–1235, https://doi.org/10.1007/s11340-014-9875-1.

[5] T.T. Nguyen, J. Yvonnet, M. Bornert, C. Chateau, Initiation and propagation of complex 3D networks of cracks in heterogeneous quasi-brittle materials: Direct comparison between in situ testing-microCT experiments, J Mech Phys Solids (2016), https://doi.org/10.1016/j.jmps.2016.06.004.

[6] Ł. Skarżyński, J. Tejchman, Experimental Investigations of Fracture Process in Concrete by Means of X-ray Micro-computed Tomography, Strain 52 (1) (2016) 26–45, https://doi.org/10.1111/str.12168.

[7] Yao W, Xu Y, Xia K. Damage Evolution During Rock Pulverization Induced by Dynamic Compressive Loading. Journal of Geophysical Research: Solid Earth 2020; 125:e2020JB019388. doi:10.1029/2020JB019388.

[8] F. Renard, Microfracturation in rocks: from microtomography images to processes, The European Physical Journal Applied Physics 60 (2) (2012) 24203, https://doi.org/10.1051/epjap/2012120093.

[9] V. Cnudde, M.N. Boone, High-resolution X-ray computed tomography in geosciences: A review of the current technology and applications, Earth Science Reviews 123 (2013) 1–17, https://doi.org/10.1016/j.earscirev.2013.04.003.

[10] I.L. Morgan, H. Ellinger, R. Klinksiek, J.N. Thompson, Examination of Concrete by Computerized Tomography, Jp 77 (1980) 23–27, https://doi.org/10.14359/6987.

[11] E.N. Landis, E.N. Nagy, D.T. Keane, S.P. Shah, in: Observations of Internal Crack Growth in Mortar Using X-ray Microtomography, Materials for the New Millennium, ASCE, 1996, pp. 1330–1336.

[12] E.N. Landis, D.T. Keane, X-ray microtomography for fracture studies in cement-based materials, Spie (1999).

[13] E.N. Landis, E.N. Nagy, D.T. Keane, Microstructure and fracture in three dimensions, Engineering Fracture Mechanics 70 (7-8) (2003) 911–925, https://doi.org/10.1016/S0013-7944(02)00157-1.

[14] S. Diamond, E. Landis, Microstructural features of a mortar as seen by computed microtomography, Mater Struct 40 (9) (2007) 989–993, https://doi.org/10.1617/s11527-006-9194-9.

[15] J.S. Lawler, D.T. Keane, S.P. Shah, Measuring Three-Dimensional Damage in Concrete under Compression, ACI Materials Journal 98 (2001) 465–475, https://doi.org/10.14359/10847.

[16] Hild F, Roux S, Bernard D, Hauss G. On the use of 3D images and 3D displacement measurements for the analysis of damage mechanisms in concrete-like materials. International Conference on Fracture Mechanics of Concrete and Concrete Structures. 2013.

[17] C. Loeffler, Q. Sun, B. Williams, B. Martin, W. Heard, X.u. Nie, A Damage-Based Approach to Determine the Dynamic Increase Factor for Concrete, J Dynamic Behavior Mater 6 (2) (2020) 159–169, https://doi.org/10.1007/s40870-019-00232-9.

[18] E.N. Landis, E.N. Nagy, D.T. Keane, G. Nagy, Technique to Measure 3D Work-of-Fracture of Concrete in Compression, J Eng Mech 125 (6) (1999) 599–605, https://doi.org/10.1061/(ASCE)0733-9399(1999)125:6(599).

[19] Mahabadi OK, Randall NX, Zong Z, Grasselli G. A novel approach for micro-scale characterization and modeling of geomaterials incorporating actual material heterogeneity. Geophys Res Lett 2012;39:n/a–n/a. doi:10.1029/2011GL050411.

[20] E.E. Bernardes, E.V. Mantilla Carrasco, W.L. Vasconcelos, A.G. de Magalhães, X-ray microtomography (μ-CT) to analyze the pore structure of a Portland cement composite based on the selection of different regions of interest, Construction and Building Materials 95 (2015) 703–709, https://doi.org/10.1016/j.conbuildmat.2015.07.128.

[21] M. Henry, I.S. Darma, T. Sugiyama, Analysis of the effect of heating and re-curing on the microstructure of high-strength concrete using X-ray CT, Construction and Building Materials 67 (2014) 37–46, https://doi.org/10.1016/j.conbuildmat.2013.11.007.

[22] S. Fan, M. Li, X-ray computed microtomography of three- dimensional microcracks and self-healing in engineered cementitious composites, Smart Materials and Structures 24 (2014) 1–14, https://doi.org/10.1088/0964-1726/24/1/015021.

[23] S. Brisard, M. Serdar, P.J.M. Monteiro, Multiscale X-ray tomography of cementitious materials_ A review, Cement and Concrete Research 128 (2020), 105824, https://doi.org/10.1016/j.cemconres.2019.105824.

[24] Girgin ZC, Arioglu N, Journal EAAS, 2007. Evaluation of strength criteria for very-high-strength concretes under triaxial compression. HiPerMat n.d.

[25] Williams EM, Graham SS, Reed PA, Rushing TS. ERDC/GSL TR-09-22 Laboratory characterization of Cor-Tuf concrete with and without steel fibers. 2009.

[26] Wang YB, Liew JY, Journal SLAM, 2016. EBSCOhost | 112480065 | Experimental Study of Ultra-High-Strength Concrete under Triaxial Compression. ACI Materials Journal n.d.

[27] R. Sovják, F. Vogel, B. Beckmann, Triaxial compressive strength of ultra high performance concrete, Acta Polytech 53 (2013) 901–905, https://doi.org/10.14311/AP.2013.53.0901.

[28] C. Poinard, E. Piotrowska, Y. Malecot, L. Daudeville, E.N. Landis, Compression triaxial behavior of concrete: the role of the mesostructure by analysis of X-ray tomographic images, European Journal of Environmental and Civil Engineering 16 (sup1) (2012) s115–s136, https://doi.org/10.1080/19648189.2012.682458.

[29] Williams BA, Sun Q, Heard WF, Loeffler CM, Graham SS, Vankirk G, et al. Investigation of strain-rate and pressure effects for high-strength concrete using a novel large-diameter triaxial Kolsky bar technique. Cement and Concrete Composites 2021;121. doi:10.1016/j.cemconcomp.2021.104085.

[30] K. Ragalwar, W.F. Heard, B.A. Williams, R. Ranade, Significance of the particle size distribution modulus for strain-hardening-ultra-high performance concrete (SH-UHPC) matrix design, Construction and Building Materials 234 (2020) 117423, https://doi.org/10.1016/j.conbuildmat.2019.117423.

[31] Williams BA, Heard WF, Martin BE, Loeffler CM, Nie X. Large-Diameter Triaxial Kolsky Bar for Evaluating Very-High-Strength Concrete. Dynamic Behavior of Materials, Volume 1, Cham: Springer, Cham; 2020, pp. 115–8. doi:10.1007/978-3-030-30021-0_20.

[32] Williams BA, Heard WF, Graham SS, Martin BE, Loeffler CM, Nie X. Mechanical Response and Damage Evolution of High-Strength Concrete Under Triaxial Loading. Dynamic Behavior of Materials, Volume 1, Cham: Springer, Cham; 2019, pp. 69–71. doi:10.1007/978-3-319-95089-1_9.

[33] Vankirk G, Heard WF, Frank A, Hammons M, Roth MJ. Residual Structural Capacity of a High-Performance Concrete. Dynamic Behavior of Materials, Volume 1, Cham: Springer, Cham; 2019, pp. 233–6. doi:10.1007/978-3-319-95089-1_42.

[34] G. Vankirk, A.O. Frank, M.J. Roth, in: The Effects of Concrete Damage on Projectile Penetration: A Computational Study using the HRB Model and the EPIC Hydrocode, International Symposium for the Interaction of Munitions with Structures, Panama City Beach, 2019, pp. 1–14.

[35] C09 Committee, ASTM C42: Standard Test Method for Obtaining and Testing Drilled Cores and Sawed Beams of Concrete, ASTM International, Westt Conshohocken, PA, 2020.

[36] Beatty HB, Graham SS, Moxley RE, Akers SA, Reed PA. ERDC/GSL TR-12-26 Laboratory Characterization of Adobe (Scottsdale) 2012.

[37] E.M. Williams, S.A. Akers, P.A. Reed, ERDC/GSL TR-05-16 Laboratory Characterization of Fine Aggregate Cementitious Material, U.S. Army Engineer Research and Development Center, Vicksburg, MS, 2005.

[38] B. Williams, W. Heard, S. Graham, X.u. Nie, Effect of specimen geometry on triaxial compressive response of high-strength concrete, Construction and Building Materials 244 (2020) 118348, https://doi.org/10.1016/j.conbuildmat.2020.118348.

[39] Bruker Software for X-Ray Microscopy & Micro Computed Tomography n.d.

[40] A. Madra, N.E. Hajj, M. Benzeggagh, X-ray microtomography applications for quantitative and qualitative analysis of porosity in woven glass fiber reinforced thermoplastic, Composites Science and Technology 95 (2014) 50–58, https://doi.org/10.1016/j.compscitech.2014.02.009.

[41] A. Madra, J. Adrien, P. Breitkopf, E. Maire, F. Trochu, A clustering method for analysis of morphology of short natural fibers in composites based on X-ray microtomography, Composites Part a: Applied Science and Manufacturing 102 (2017) 184–195, https://doi.org/10.1016/j.compositesa.2017.07.028.

[42] X. Lu, C.-T. Hsu, Behavior of high strength concrete with and without steel fiber reinforcement in triaxial compression, Cement and Concrete Research 36 (9) (2006) 1679–1685, https://doi.org/10.1016/j.cemconres.2006.05.021.

[43] Mindess S, Young FJ, Darwin D. Concrete. 2nd ed. Upper Saddle River, NJ: Pearson Education, Inc; 2003.
[44] C09 Committee. ASTM C39: Standard test method for compressive strength of cylindrical concrete specimens. West Conshohocken, PA: ASTM International; 2018. doi:10.1520/C0031_C0031M.
[45] Imran I, Pantazopoulou S. Experimental Study of Plain Concrete under Triaxial Stress. ACI Structural Journal n.d.;93:589–601.